

Simulation of Hypersonic Conditions Over a Blunt Body Using a Hybrid Rocket with Nitrogen Plume Cooling

Joshua R. Sorenson*, Stephen A. Whitmore†, Jared S. Coen‡, Jaron T. Dowdy§, and Ryan J. Thibaudeau¶
Utah State University, Logan, UT 84322

Reliable, ground-based simulations of high-enthalpy flows are crucial for hypersonic flight vehicle development, as they allow detailed assessment of aerodynamic behavior, heat transfer, and material durability. Yet, current hypersonic test facilities, such as shock tunnels and arc-heated wind tunnels, have notable constraints: they are costly, require significant preparation time, and are not readily available for testing early-stage designs. This restricted access slows down innovation and limits experimentation with novel hypersonic technologies. This paper introduces an alternative approach that employs hybrid rocket propulsion to generate high enthalpy flows, simulating hypersonic flight conditions. The presented method adapts a laboratory-scale green-propellant hybrid rocket into a gas generator, channeling its exhaust directly onto the leading edge of a subscale test article representing the forebody of a hypersonic craft. The resulting system produces a partial continuum flow around the test object, allowing simultaneous simulation of both the enthalpy and dynamic pressure found in stratospheric hypersonic flight—something traditional arc-jet facilities do not offer. During experiments, the motor performance characteristics, surface pressure distributions, and leading-edge temperatures on the test article were measured and logged. Initial results showed unexpectedly high plume temperatures with impinging enthalpy exceeding those typical of Mach 10 flight. By introducing gaseous nitrogen at the nozzle exit plane, the plume's temperature is significantly reduced, enabling the recreation of flow enthalpies consistent with Mach 6 through 9 flight conditions. As an added benefit, the nitrogen injection changed the exhaust plume's properties, making experiments more like real atmospheric flight. The presented results demonstrate this method to be effective in providing an affordable, practical platform for early hypersonic research and supports design and endurance studies without expensive facilities. Such affordable options are valuable for maturing innovative concepts prior to undertaking expensive, high-fidelity tests.

Nomenclature

\dot{m}	= mass flow rate, kg/s
C_d	= discharge coefficient
A	= area, m^2
P	= pressure, Pa
γ	= specific heat ratio
R	= specific gas constant, $J/kg \cdot K$
T	= temperature, K
H	= total enthalpy, MJ/s
MW	= molecular weight, amu

*Graduate Research Assistant, Mechanical and Aerospace Engineering, Utah State University, 4130 Old Main Hill, Logan, UT 84322, Student Member.

†Professor, Mechanical and Aerospace Engineering, Utah State University, 4130 Old Main Hill, Logan, UT 84322, Associate Fellow.

‡Graduate Research Assistant, Mechanical and Aerospace Engineering, Utah State University, 4130 Old Main Hill, Logan, UT 84322, Student Member.

§Undergraduate Research Assistant, Mechanical and Aerospace Engineering, Utah State University, 4130 Old Main Hill, Logan, UT 84322, Student Member.

¶Graduate Research Assistant, Mechanical and Aerospace Engineering, Utah State University, 4130 Old Main Hill, Logan, UT 84322, Student Member.

c_p	=	specific heat at constant pressure, J/K
a	=	amplitude
λ	=	wavelength, nm
t	=	time, s
SNR	=	signal-to-noise ratio
S	=	signal
N	=	noise
ϵ	=	conditioning coefficient
Υ	=	transfer function
B	=	spectral radiance, $W/sr \cdot m^3$
h_p	=	Planck constant, $J \cdot s$
k_B	=	Boltzmann constant, $J/K \cdot mol$
w	=	scaling factor
b	=	Wien's displacement constant, $\mu m \cdot K$
v	=	velocity, m/s
$K.E.$	=	kinetic energy, J
J	=	enthalpy of decomposition, $kJ/g \cdot mol$
R_u	=	universal gas constant, $J/kg \cdot K$

Subscripts

0	=	stagnation
GN_2	=	nitrogen
m	=	mean
t	=	true
e	=	exit
2	=	mixed flow
c	=	chamber

Acronyms

CFD	=	Computational fluid dynamics
USU	=	Utah State University
PRL	=	Propulsion Research Laboratory
TRL	=	Technology readiness level
GOX	=	gaseous oxygen
ABS	=	acrylonitrile butadiene styrene
GN_2	=	gaseous nitrogen
HVPS	=	high-voltage power supply
P&ID	=	piping and instrumentation diagram
BLAST	=	Battery Limits and Survivability Testing
NIR	=	near-infrared
CEA	=	Chemical Equilibrium with Applications
O/F	=	oxidizer-to-fuel
FADS	=	Flush Airdata Sensing

I. Introduction

THE Department of Defense is developing endo-atmospheric hypersonic vehicles designed to remain in the stratosphere for long periods. Sustained hypersonic flight poses unique technical challenges rarely seen in other flight regimes such as chemical dissociation and material ablation. Although recent advancements in analytical modeling methods like Computational Fluid Dynamics (CFD) have been significant and simulations can offer reliable preliminary assessments, they remain insufficient for fully capturing the intricate physical phenomena associated with hypersonic flight. Accurate ground testing plays a pivotal role in the development of re-entry capsules, hypersonic missiles, and spaceplanes. However, conventional facilities like shock tunnels and arc heaters are limited in various areas. High-enthalpy testing is costly and limited by the small number of existing facilities, restricting innovation in hypersonic technologies.

This paper investigates cost-effective solutions for high-enthalpy testing, examining prevailing industry practices and their inherent constraints. It proposes an innovative alternative: employing a laboratory-scale, green-propellant

hybrid rocket as a gas generator. The exhaust plume from the rocket is directed at the leading edge of a small test article to replicate conditions experienced by the forebody of a hypersonic vehicle. The paper details the technology developed at Utah State University's (USU) Propulsion Research Laboratory (PRL) and presents new evidence demonstrating the system's data collection capabilities.

This method can be applied to sensor development, code validation, materials evaluation, and survivability testing. It enables simultaneous simulation of stratospheric hypersonic-flight enthalpy and dynamic pressure levels, which are not possible with current arc-jet facilities. Once mature, this methodology will offer cost-effective, rapid highenthalpy testing and accelerate the advancement of lower Technology Readiness Level (TRL) concepts before transitioning to more expensive, high-fidelity test facilities.

II. Background

Hypersonic conditions are defined by flows in which molecular dissociation and atomic and molecular ionization occur. Such flows typically take place at or above Mach 5, thereby establishing the hypersonic flight regime as Mach 5 and higher. The concept of hypersonic flight emerged in the 1930s and soon attracted significant scientific interest worldwide. It was only in 1944, with Germany's launch of the V-2 rocket—achieving speeds exceeding Mach 5 during ascent—that those theoretical concepts transitioned into practical achievement. Between 1959 and 1968, the X-15 program reached Mach 6.7 and gathered critical data on aerodynamic heating, material response, and flight control, which advanced U.S. capabilities in ground-based testing, new material development, and sophisticated simulation of hypersonic flows [1].

A. Ground-Based Hypersonic Testing

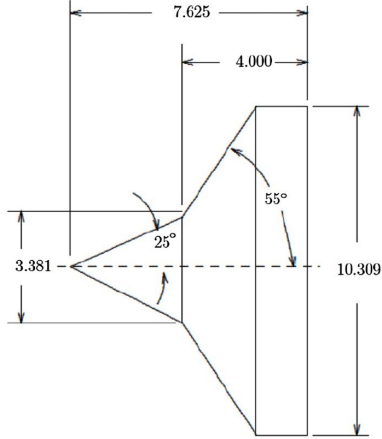
Ground-based hypersonic test facilities are usually the last step in experimental testing before hypersonic vehicles go into flight. Two crucial aspects of these tests are flow duration and flow velocity. Although these facilities can create conditions that match the Mach numbers experienced during flight, it's important to remember that Mach number is tied to the local speed of sound, so test velocities might not exactly mimic those encountered in actual flight. Gu et al. [2] compared different types of hypersonic test setups—continuous, blowdown, gun tunnels, adiabatic compression units, hotshot tunnels, reflected shock tunnels, and expansion tunnels—focusing on each facility's flow duration and velocity. Shock tunnels and expansion tubes can reach the greatest velocities and enthalpies, but only provide short test windows (from microseconds to milliseconds). Blowdown, gun, and hotshot tunnels allow for longer tests (milliseconds to seconds) but operate at lower velocities and, except for hotshot tunnels, cooler temperatures. Reflected shock tunnels offer a middle ground between duration and velocity. Because no facility can perfectly recreate all flight conditions at once, researchers choose the facility based on the unique requirements of their study.

B. Hypersonic Flow Simulation Using Analytical Models and Computational Fluid Dynamics

Hypersonic flight poses major aerodynamic, thermal, and material challenges. Classical theories using perfect-gas assumptions are useful for quick design but fail at high enthalpy where shock waves trigger nonequilibrium effects like dissociation and ionization. As a result, these classical theories underestimate heat transfer and cannot represent key phenomena or account for radiative effects [1]. CFD modeling is also limited in capturing complex chemical and thermal processes under hypersonic conditions. Therefore, highenthalpy ground tests remain essential for advancing hypersonic technology.

The first commercially available CFD tool, PHOENICS, debuted in 1977 [3]. Since then, CFD software has grown and evolved into the powerful tool used today. CFD software uses advanced numerical analysis and data structures to simulate fluid flow over 3D-modeled objects. In recent years, CFD has been used to simulate hypersonic flows. Although CFD simulations have come a long way since 1977, parameters of certain body geometries are still not accurately predicted. The necessity for flow validation outside of CFD simulations of complex geometries is apparent.

In an assessment to predict CFD capabilities for modeling low and high enthalpy flows, Knight et al. [4] performed experiments for two bodies. The experimental setup included a double cone and a cylinder configuration. The configurations are shown in Fig. 1. Experimental data was collected and compared against CFD simulations for low and highenthalpy flows. For the highenthalpy set of experiments, results showed that the CFD estimations for the double cone accurately predicted surface pressure and heat transfer. The results for the cylinder indicated that CFD predictions closely matched the measured surface pressure; however, the heat transfer values were consistently underestimated.



(a) Double Cone



(b) Supported Cylinder

Fig. 1 Test configurations used for CFD evaluation by Knight et al. [4].

C. Building Upon Previous Work

The following work extends the methodology established by Whitmore et al. [5], leveraging a hybrid rocket motor employed as a gas generator to replicate hypersonic flight conditions. This study showed that a lab-scale hybrid rocket motor can serve as a cost-effective gas generator for high-enthalpy testing of hypersonic vehicle components. The experimental configuration utilized a repurposed 75-mm hybrid thruster, combusting gaseous oxygen (GOX) and acrylonitrile butadiene styrene (ABS), to generate a high-enthalpy exhaust plume. The test specimen depicted in Fig. 2 was instrumented with eleven pressure ports and dual-band fiber-optic sensors [6] to measure the impingement plume temperature. The exhaust plume impinged upon a wedge-shaped test article with a 12.5° half angle and a 0.5-in. radius blunted leading edge composed of hexagonal boron nitride. Positioned 16 inches from the nozzle exit, the setup achieved a partially continuum flow field, yielding impingement Mach numbers near 1.5 and temperatures ranging from 1790 °C to 1960 °C—conditions that correspond to stratospheric flight at Mach 8 and above. Figure 3 shows the test article immersed in the high enthalpy exhaust plume during a hot fire.

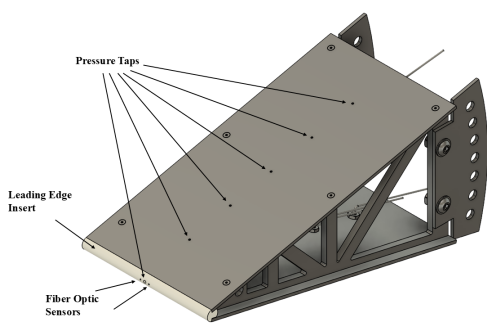


Fig. 2 2D test article used for initial high-enthalpy tests of Whitmore et al. [5].

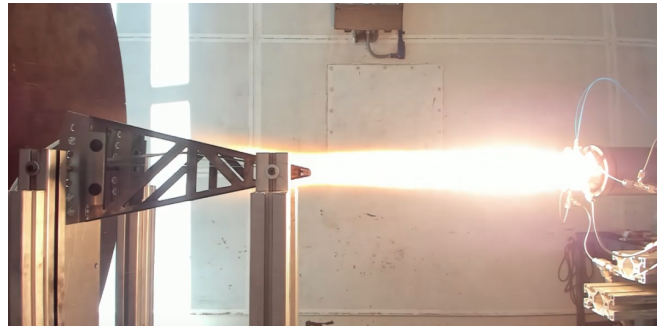


Fig. 3 2D test article immersed in high-enthalpy exhaust plume.

The previous method resulted in plume temperatures and impingement enthalpies higher than expected. To address this issue, the current study adds an injection cap at the motor's aft end to introduce a secondary injection of gaseous nitrogen (GN_2). The added GN_2 flow effectively cools the plume and generates flow enthalpies for Mach 5 through 8 conditions while also making the exhaust plume composition closer to free air. Initial validation with GN_2 injection used the previously referenced hypersonics test article of Fig. 2. This 2D shape was later replaced by a Rankine-like [7] blunt body with pressure taps and fiber optic sensors. Results from the blunt-body tests will be reported in a later section of this paper.

III. Methodology

This section describes the experimental and analytical methods that were used to perform the high-enthalpy testing campaign. The experimental hardware will be described in detail first, followed by a description of the analytical methods.

A. Test Hardware

This subsection will discuss in detail the thrust chamber and its legacy, the GN_2 injection manifold, the measurement system, the 2D and blunt body test articles, and the test article instrumentation system.

1. Thrust Chamber

The gas-generator used in this test regime was developed from a legacy 75-mm, 200 N hybrid rocket motor that had been extensively tested in the USU PRL [5, 8, 9]. As previously mentioned, this motor burns GOX and 3D printed ABS as propellants. Figure 4 shows a cross-sectional view of the thrust chamber, featuring the major system components: (1) chamber pressure fitting, (2) motor cap with single-port injector, (3) 3D printed ABS ignitor cap with embedded electrodes, (4) insulating liner, (5) 3D printed fuel grain, (6) motor case, (7) nozzle retainer, and (8) nozzle.

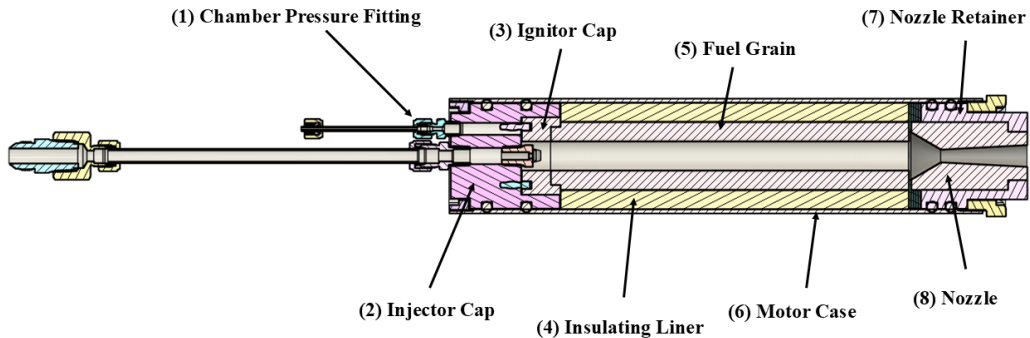


Fig. 4 Cross-sectional view of the gas-generator system components.

The thrust chamber technology relies on USU's patented low-energy arc-ignition system [10] which leverages the unique electrostatic breakdown characteristics of certain 3D printed thermoplastics. Past studies show that ABS exhibits the best properties required for successful ignition [11]. Three-dimensional printing using fused deposition modeling changes the electrical breakdown properties of the plastic material, and when printed materials are presented with an inductive electrical potential, electrical arcing along the layered surface pyrolyzes material. Whitmore et al. [12] describes this arc-pyrolysis phenomenon in detail.

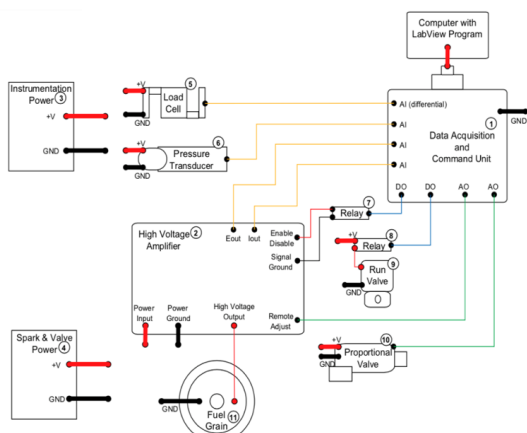


Fig. 5 Ignition System Electronics Layout.

Figure 5 presents a schematic of the ignition system electronics. The ignition system power processing unit is based on the Advanced Energy Systems UltraVolt® line of high-voltage power supplies (HVPS) [13]. The HVPS provides a current-limited (30 mA) high-voltage output of up to 1000 V or 30 Watts total output. Typical startup sequences require less than two joules, and once started, the system can be sequentially fired with no additional energy inputs required [14]. The only limit to the number of available restarts is the amount of fuel material present in the arc path section of the ignitor cap.

2. Nitrogen Secondary Injection Manifold

As described previously, the thrust chamber, picture by Fig. 4, was retrofitted with a manifolds ring on the aft end of the motor, allowing a secondary injection of GN_2 into the exhaust plume. Figure 6 shows this manifold configuration.

Here, four injection ports are oriented such that the injected GN_2 enters the exhaust plume orthogonal to the flow direction. The high velocity nozzle exhaust entrains the injected GN_2 where it subsequently mixes and cools the plume. Figure 7 illustrates this entrainment process. A thermodynamic model, predicting the influence of entrained GN_2 on the mixed-flow enthalpy, is presented later in this section.

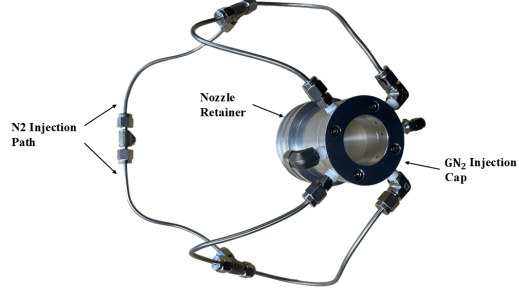


Fig. 6 3D view of GN_2 manifold fastened to the nozzle retainer.

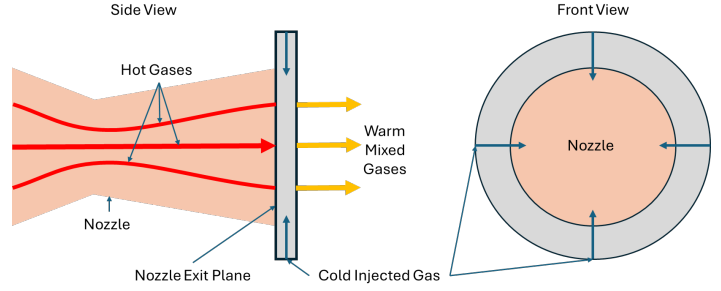


Fig. 7 Concept schematic showing mixing of GN_2 with hot plume gases.

3. Gas Generator Test Support and Measurement Systems

Figure 8 presents the piping and instrumentation diagram (P&ID) for the motor support systems used in this testing. The motor was attached to a calibrated thrust-stand with flexible mounts, enabling axial thrust transmission. Feed pressures were set manually via a pressure reducing regulator and adjusted to reach target chamber pressures. The motor instrumentation pallet connected to the control/data logging laptop with a single USB. Pre-programmed custom software handled ignition control, data acquisition, and processing for consistent test runs. All tests took place in the USU Battery Limits and Survivability Testing (BLAST) laboratory. Full details of the motor, ignition control, and supporting measurement systems are presented by Whitmore et al. [9] and Sorenson et al. [15].

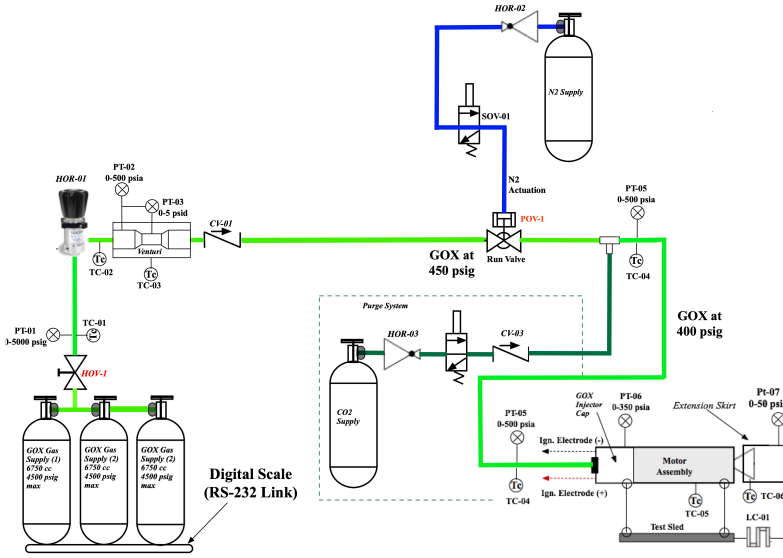


Fig. 8 USU gas-generator test support systems P&ID.

4. 2D Wedge Test Article

In the configuration of the two-dimensional test article, as illustrated in Fig. 2, a total of 11 pressure ports were installed. Five ports were positioned on each of the upper and lower surfaces, and a stagnation pressure port was

incorporated into the cylindrical leading-edge insert. Both boron nitride and stainless steel have been utilized for this leading-edge insert; however, boron nitride has demonstrated superior durability. Figure 9 illustrates the adjustable mounting system for the test article, constructed with T-slot rails. The article was positioned on a stand that allowed both vertical and horizontal adjustments, enabling precise alignment with the centerline of the nozzle. The angle of attack of the test article relative to the gas-generator axis is adjusted by differing position on the support mounts.

5. 3D Blunt Body Test Articles

As described earlier, the 2D test article was replaced by two blunt body articles that are more compatible with the axi-symmetrical flow field exiting the gas generator. The first 3D geometry was a simple blunted cone with a spherical leading surface. The second 3D geometry had a sharper bullet-like shape as the leading surface. Figure 10 illustrates these geometries. The sphere-cone blunt body had five pressure ports on its front and one fiber optic cable to measure flame temperature, while the bullet-nose blunt body featured just a single stagnation port.

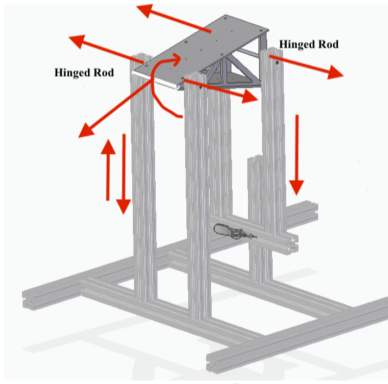


Fig. 9 2D test article assembly.

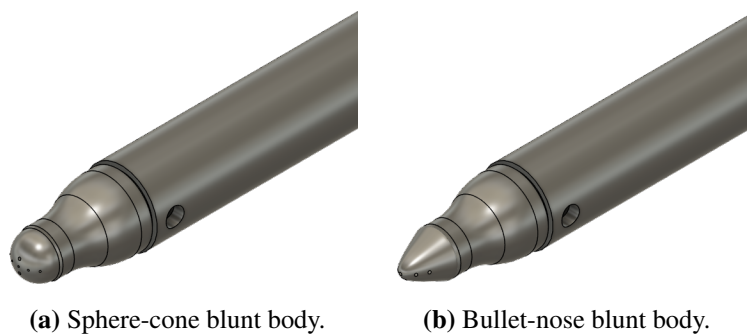


Fig. 10 Solid model assemblies of the 3D test article geometries.

6. High-Enthalpy Test Article Instrumentation Systems

The test article's instrumentation system operated independently from the motor ignition-control and data logging systems. Figure 11 shows the test article schematic. The static port pressures for the test articles were sensed using a Measurement Specialties® smart digital pressure scanner [16]. The scanner system consists of an intelligent module with 16 integral pressure transducers and a pneumatic calibration manifold. The module is interfaced through a standard 10-Base-T Ethernet communications with TCP/IP protocol. Each transducer is individually addressable. Ambient reference pressure measurements for the scanner system were sensed using a 25 psia absolute pressure transducer. The stagnation port pressure measurements were sensed using a 100 psia absolute pressure transducer. Pressure measurements were transmitted to the remotely located transducers using a section of stainless-steel tubing, transitioning to flexible silicone tubing.

In addition to the pressure sensor taps, two fiber-optic sensing cables were installed within the leading surfaces of the test article to measure incoming flow flame temperatures. For details on this optical sensing technology see Whitmore et al. [17] and Whitmore et al. [18]. In this approach, the glass fiber-optic cables, acting as radiation conduits, were inserted to look directly into the flow field core. While the tips of the fiber-optic cables were destroyed by the fire, they stayed level with the fuel port surface and continued transmitting light throughout the burn. To fully capture the black-body spectrum emitted by the combustion flame, a blended dual-spectrum approach was utilized [6]. One spectrometer was optimized for maximum sensitivity across the visible-light range, while the other was configured for optimal performance in the near-infrared (NIR) region. Visible light was measured using two spectrometers: one from ASEQ Instruments [19] and one from Broadcom Inc. [20], with each used interchangeably. For the infrared measurements, an NIR spectrometer from Broadcom Inc. [21] was used. The dual-band sensors were radiometrically calibrated, and the sensed-spectra were spliced together using an optimal Wiener filtering algorithm to perform the deconvolution. The merged spectrum is subsequently curve-fit to Planck's black-body radiation law [22], and flame temperature is calculated from associated curve-fit maxima (Wien's law [23]). For completeness, Appendix A of this paper details the calculations required to derive temperatures from the fiber optic spectra.

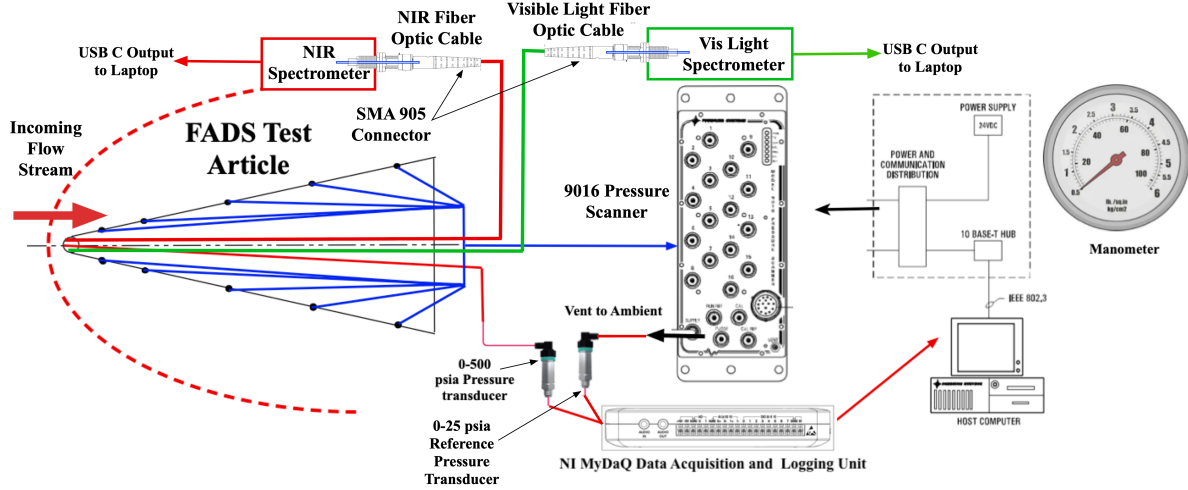


Fig. 11 Test article instrumentation and data logging system.

B. Plume Characteristics

The method of calculating downstream plume characteristics is as follows: rocket motor performance data is collected during hot fires, nozzle exit characteristics are obtained with software, final plume conditions are calculated using conservation of momentum with GN_2 addition. Temperature is also calculated as another form of verification of the Planck's Law fit. This method assumes full mixing of GN_2 with the plume and 20% nitrogen dissociation. Future work will explore using CFD to verify assumptions.

1. Nozzle Exit Characteristics

After rocket performance data is recorded, nozzle exit parameters can be calculated. Nozzle exit parameters are calculated using NASA Chemical Equilibrium with Applications (CEA) software. The rocket performance data required to obtain correct nozzle characteristics from CEA are chamber pressure, nozzle expansion ratio, oxidizer-to-fuel (O/F) ratio, a combustion temperature initial estimate, and oxidizer and fuel properties. The oxidizer properties required include the chemical formula, relative weight percent amount, and a pre-combustion temperature. The fuel properties include the chemical formula, relative weight percent amount, pre-combustion temperature, and the total enthalpy. ABS is composed of three distinct monomers. The monomers with associated weight percentages and total enthalpies are calculated using methods described by Whitmore et al. [24] and are shown in Table 2.

Table 2 Acrylonitrile Butadiene Styrene Monomer Breakdown

Monomer	Weight Percentage, %	Total Enthalpy, H (J)
$C_3H_3N_1$	13.39	98.31
C_4H_6	14.57	32
C_8H_8	72.04	63.31

It is important to note that the chamber pressure, nozzle expansion ratio, and O/F ratio will change throughout the hot fire. Because of this change over time, an array of CEA outputs for differing inputs is created. The current method interpolates between array values to obtain output data. This process is split among LabVIEW VIs and MATLAB scripts. Current efforts are being done to streamline the process and calculate all data within one software.

Key nozzle exit characteristics for flow mixing include the O/F ratio, combustion product mass flow, chamber pressure, nozzle exit pressure, and nozzle efficiency. Relevant CEA output values are nozzle exit temperature, nozzle exit pressure, gas molecular weight, specific heat at constant pressure, total enthalpy flow, and exit velocity. Thrust is measured directly with the load cell and mass flow rate is computed numerically based on sensor data and post-test measurements. Exit velocity is computed using the computed CEA array which requires chamber pressure and nozzle area ratios.

2. Nitrogen Injector Characteristics

The GN_2 injection occurs orthogonal to the flow through four ports. Key GN_2 injection port characteristics for flow mixing include stagnation pressure, stagnation temperature, ambient pressure, port discharge coefficient, orifice diameter, mass flow rate, specific enthalpy, total enthalpy flow, and ratio of specific heats. The port discharge coefficient is calibrated from system cold-flow tests. From the discharge coefficient and standard compressible orifice relations, the mass flow rate is calculated. The flow is observed to be choked at the port, so the mass flow rate equation is given by Eq. (1). Total mass flow rate is calculated by multiplying the port-specific mass flow rate by the number of ports.

$$\dot{m} = C_d A P_0 \sqrt{\frac{\gamma_{\text{GN}_2}}{R_{\text{GN}_2} T_0} \left(\frac{2}{\gamma_{\text{GN}_2} + 1} \right)^{\frac{\gamma_{\text{GN}_2} + 1}{\gamma_{\text{GN}_2}}}} \quad (1)$$

3. Mixed Flow Characteristics

The mixture of hot gas and GN_2 is calculated using conservation of mass and total enthalpy. The combined stream enthalpy is used to solve for the combined flow temperature. This combined flow temperature provides another anchor to the stagnation temperature calculated from the fiber-optics measurements. The one-dimensional enthalpy balance model is derived in Appendix B.

4. Mixed Flow Calculation Example

Figure 12 shows the results of an example calculation using the above-described mixed-flow enthalpy model. This example illustrates the effectiveness of the secondary GN_2 injection. Plotted are the chamber and nozzle exit temperatures (Fig. 12a) and the total power of the exhaust plume at the exit plane of the motor (Fig. 12b). Figure 12a also plots the CEA-derived temperature values as a function of O/F ratio for 5 different chamber pressure levels (80, 125, 250, 350, and 450 psia). Similarly, Fig. 12b plots the exhaust plume energies including the total stagnation enthalpy, the exit plane static enthalpy, and the exhaust plume kinetic energy. In Fig. 12, the solid black symbols show CEA-derived conditions at an O/F ratio of 1.9, chamber pressure of 235 psia, exhaust mass flow of 60 g/sec, and combustion efficiency of 0.975. The solid red symbols show the mixed-flow conditions assuming a secondary GN_2 injection mass flow rate of 25 g/sec.

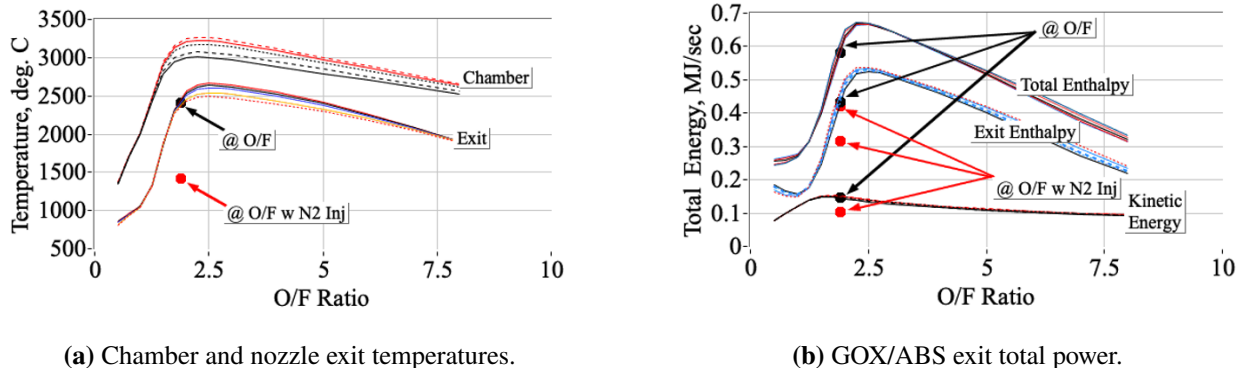


Fig. 12 Example mixed flow calculations using the 1D enthalpy balance model.

It is important to note that because of the secondary injection, the nozzle exit temperature has decreased from approximately 2400 °C initially down to roughly 1400 °C. In a similar fashion, the total flow enthalpy (power) has decreased from about 0.58 MJ/sec to roughly 0.32 MJ/sec. Table 3 Summarizes the mixed-flow calculations for this example. Although the mixed flow exhaust parameters differ from those of pure air, the blended flow parameters are still similar to those of the stand-alone GOX/ABS exhaust plume properties.

IV. Test Results

A total of 22 tests have been completed as a part of this testing regime. To verify functionality of the system and work out errors, nine initial tests without a test article were performed. Seven tests were performed with the wedge test

Table 3 Mixed Flow Analysis Example Summary

Parameter	Exit Plume (CEA)	GN ₂ Injection	Mixed Flow
Mass flow rate (g/s)	60	25	85
T_e (°C)	2413	30	1430
Total enthalpy, H (MJ/s)	0.583	0.008	0.318
γ	1.142	1.40	1.186
MW (kg/kg-mol)	23.65	28.06	24.76
C_p (J/kg-K)	2827.4	1040	2141.2
R (J/kg-K)	351.6	296.3	335.8

article, one test was performed with the sphere-cone blunt body, and three tests were performed with the bullet-nose blunt body. The following sections highlight the preliminary testing and test results from two 2D wedge tests and one sphere-cone test. The tests completed with the bullet-nose blunt body did not yield spectra results and therefore, will not be discussed in this section.

A. Preliminary Testing

Preliminary static tests without GN₂ injection were conducted to characterize the baseline plume. Using a setup similar to [5], the motor produced a plume temperature of approximately 3200 °C, resulting in Mach numbers exceeding 8, as calculated from pressure ratios. These conditions were too hot for simulating Mach 5 through 8, confirming the need for plume cooling. Fiber optic measurements at the exit plane of the nozzle indicated a combustion efficiency of 95%, consistent with prior results [17].

Initial flow visualization attempts using a green-light filter, as in [5], were less effective due to suboptimal filter opacity. These findings validate the hybrid rocket's capability for high-enthalpy flow generation and highlight the necessity of GN₂ injection for achieving target Mach numbers.

Figure 13 shows images from a preliminary test of the secondary GN₂ injection system. Figure 13a shows the standard exhaust plume with no injection. Note the strong, very bright plume with visible "shock diamonds." Figure 13b shows the plume image while the secondary injection is active. Note the lower optical-intensity of the plume, as well as the plume spread and disappearance of the shock diamonds.

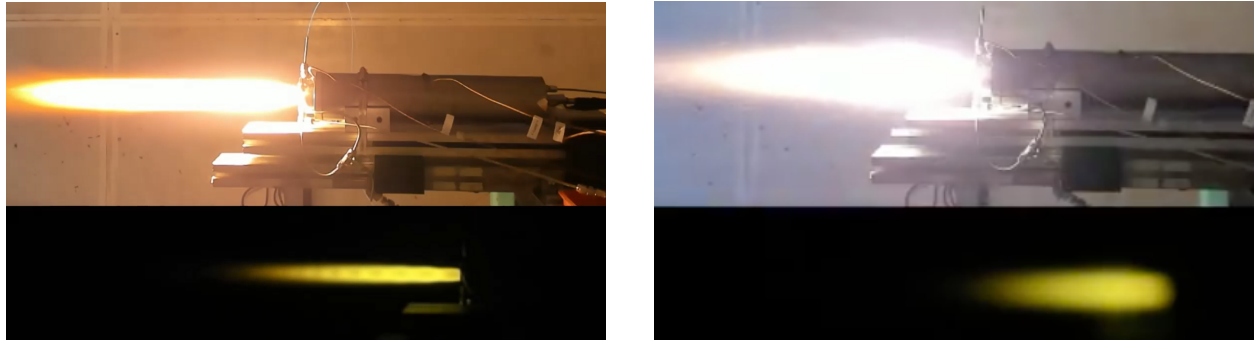


Fig. 13 Preliminary hot-fire images showing the effect of the secondary GN₂ injection system on the hybrid rocket exhaust plume.

B. Example Test Results

This section summarizes results from three gas-generator tests: two with a 2D wedge article and one with a 3D sphere-cone article. Both articles were initially tested with a four-second burn. The second 2D test extended the burn time to 10 seconds, but this longer burn duration did not significantly affect outcomes. Comparisons cover gas-generator performance, surface pressures, and optically measured leading edge/surface flow temperatures.

1. 2D Wedge Test Article

Figure 14 provides a summary of the short-duration (four-second) hot-fire test conducted with the 2D test article, featuring secondary GN_2 injection. During the experiment, the gas generator initially operated at full enthalpy without secondary injection for the first second, transitioned to three seconds with GN_2 injection, and concluded with one final second of full enthalpy flow. Notably, Fig. 14a displays an overlay of ambient pressure, Flush Airdata sensing (FADS) leading edge stagnation pressure, nozzle exit pressure, gas-generator chamber pressure, and secondary injection pressure. Figure 14b presents the impingement Mach number obtained from the test article's pressure data. In Fig. 14c, calculated CEA-derived flame and exit temperatures are plotted alongside the optically sensed leading edge temperature of the test article. Lastly, Fig. 14d illustrates that the GN_2 injection mass flow was about half the mass flow of the exhaust plume.

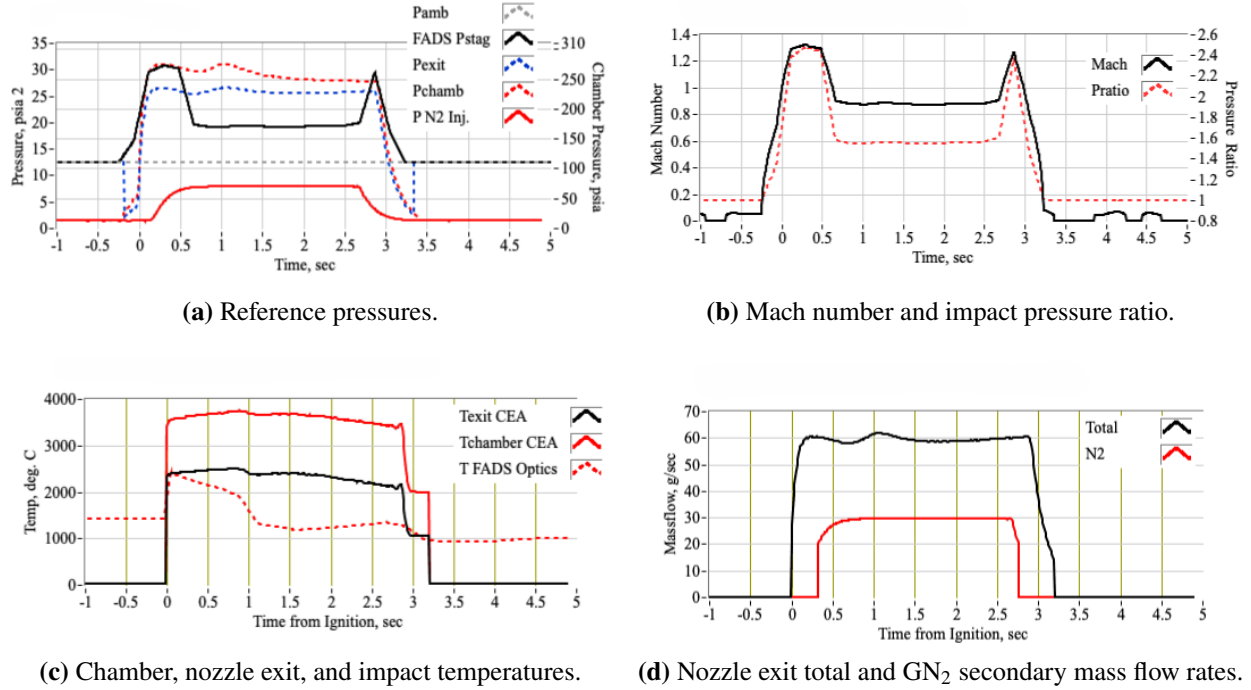
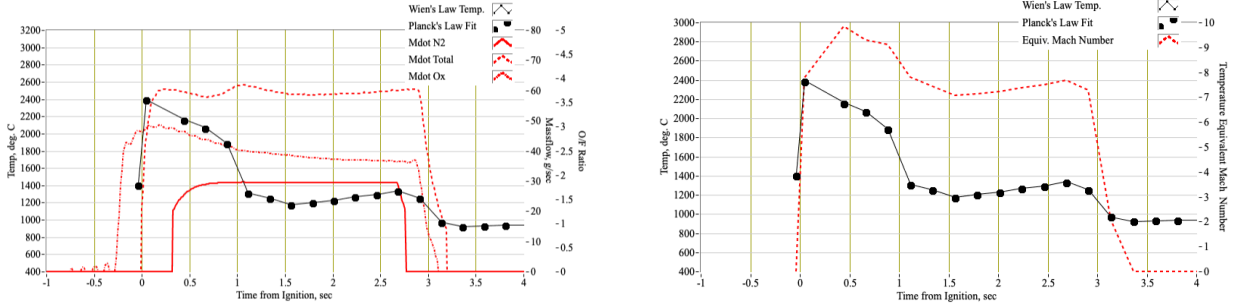


Fig. 14 Summary of the 2D test article hot-firing, four second burn, full enthalpy flow followed by GN_2 injection.

Figure 15 presents the optically sensed temperatures corresponding to the data of Fig. 14. Figure 15a compares optically measured temperatures against the three different mass flow rates: Nozzle exit total, GOX, and GN_2 . At combustion onset, the leading-edge impingement temperature is around 2400°C and drops to below 1400°C when GN_2 flow starts. These values are consistent with the blended-flow enthalpy analysis in Fig. 12. Figure 15b shows a comparison between leading edge impingement temperatures and the 'effective' Mach number—the specific value that would produce these flow temperatures on a hypersonic vehicle's leading edge during flight in the outer stratosphere at about 24.5 km altitude (80,000 ft). The initial Mach numbers are about 10 but decrease to below 8 once GN_2 flow begins. The time history of the Mach number, determined using flow temperature, can be compared with the actual Mach number of Fig. 14b. This true impingement Mach number is 1.3 during full enthalpy flow but falls to subsonic levels when GN_2 flow begins.

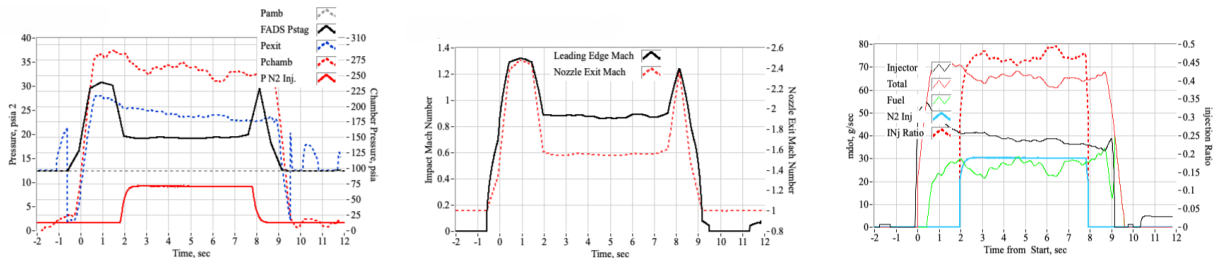
Figure 16 shows a condensed-format comparison of hot-firing results using the 2D test article with an extended burn time of 10 seconds. Figures 16a–16e present pressure, Mach number, and mass flow rate plots, and Fig. 17f compares optically measured temperatures along with the effective Mach number calculation. The test article was shifted 25% farther downstream to allow for a longer burn time, resulting in a lower leading edge impingement temperature at combustion onset than shown in Fig. 14. Here, temperatures start at around 2000°C , dropping to about 900°C when GN_2 flow starts. For this test, the initial impingement Mach numbers are about 9, but decrease to around 6.5 once GN_2 flow begins. For comparison, the true impingement Mach number is 1.3 during full enthalpy flow, but it falls to subsonic levels when GN_2 flow begins.



(a) Best-fit spectrum temperatures compared to gas-generator mass flow rate.

(b) Best-fit spectrum leading-edge temperatures with equivalent Mach number versus time.

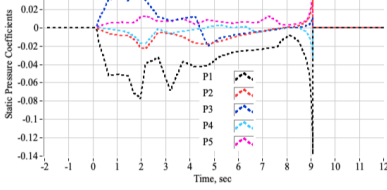
Fig. 15 Comparing optically sensed leading-edge flow temperatures against gas-generator mass flow data.



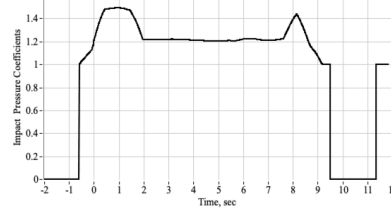
(a) Reference pressures.

(b) Mach numbers.

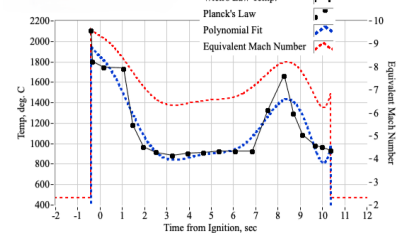
(c) Mass flow rates.



(d) FADS upper surface C_p overlay.



(e) FADS stagnation port C_p .



(f) Impingement temperature.

Fig. 16 Summary of 2D test article hot-firing, 10-second burn, full-enthalpy flow followed by GN₂ injection.

2. 3D Sphere-Cone Test Article

Figure 17 presents a similar, condensed-format data comparison for the 3D sphere-cone test article. For this test, performed at a very close range, the GN₂ secondary flow is active for the entire burn. The impingement temperatures, which range from 1300 °C to 1900 °C, are significantly lower than those observed under full-enthalpy conditions, as depicted in Figs. 14 and 15. Even though GN₂ flow remains active throughout the burn, flow temperatures are significantly higher than those shown in Figs. 14 and 15 with GN₂ active. This conflicting result likely arises from three factors: GN₂ flow cools the nozzle exit flame, the 3D shape relieves thermal stresses of incoming high-enthalpy flow [25], and the test article's position—70% closer to the nozzle exit than before—enables higher incoming flow enthalpy. The actual impingement Mach number is about 1.4 (supersonic even with GN₂ flow), while the "effective" Mach numbers range initially from just above 9.5 down to about Mach 8. The data presented by Figs. 14–17 show that by adjusting GN₂ flow, probe shape, and test article position, the leading edge/surface impingement enthalpies and effective Mach numbers can be varied widely.

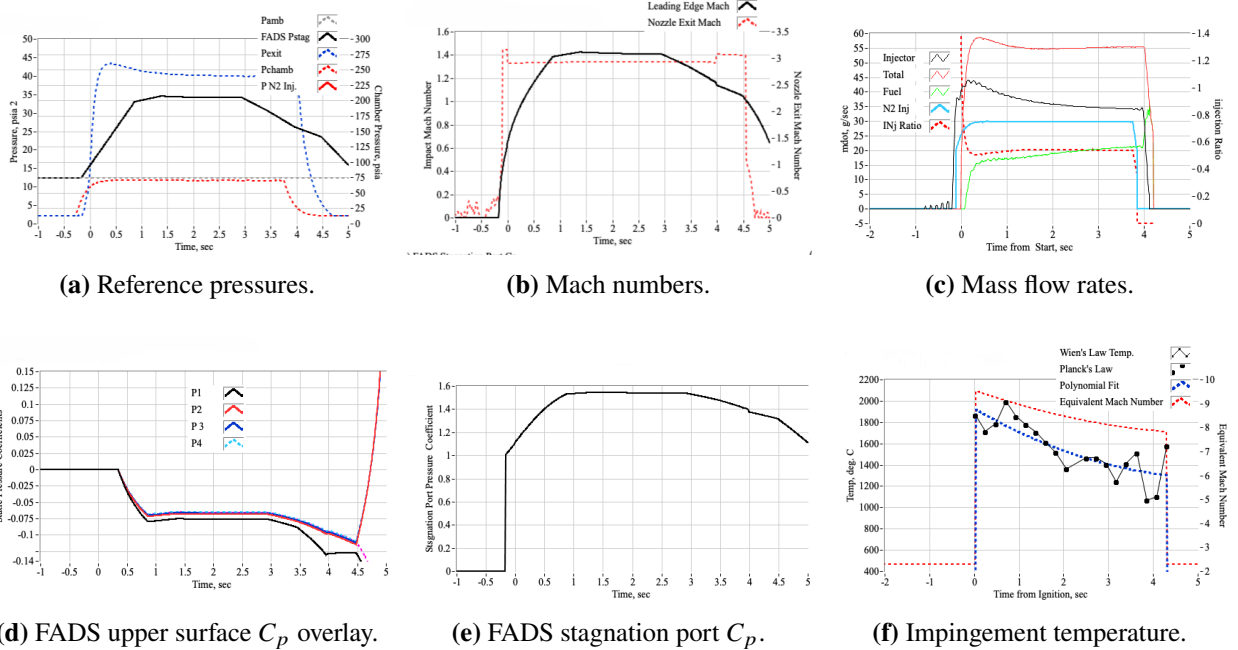


Fig. 17 Summary of 2D test article hot-firing, 10-second burn, full-enthalpy flow followed by GN₂ injection.

V. Conclusion

This study has developed and demonstrated a novel, low-cost ground-testing methodology capable of simultaneously replicating the total enthalpy and dynamic pressure levels encountered during sustained stratospheric hypersonic flight. By repurposing a laboratory-scale, green-propellant hybrid rocket as a high-enthalpy gas generator and introducing a simple, yet highly effective secondary gaseous nitrogen (GN₂) injection system at the nozzle exit plane, the thermal environment of the baseline exhaust plume was controllably reduced from conditions representative of Mach >8 flight to a tunable range corresponding to Mach 5–8 at 20–30 km altitude. This was achieved while preserving a partially continuum flow field around the test article, a capability that traditional arc-jet facilities cannot provide. Key accomplishments of the investigation include:

- Successful integration of a four-port orthogonal GN₂ injection manifold onto a legacy 75-mm GOX/ABS hybrid rocket, enabling real-time plume cooling and compositional tailoring.
- Development and validation of a one-dimensional mixed-flow enthalpy model that accurately predicts post-injection stagnation temperature and total enthalpy using measured motor performance and calibrated injector mass flow — predictions that were independently corroborated by dual-band fiber-optic pyrometry.
- Demonstration of three distinct test-article geometries (2D wedge, sphere-cone blunt body, and bullet-nose blunt body) immersed in the modified plume, with measured leading-edge stagnation temperatures ranging from about 1300 °C to about 1900 °C and effective flight-equivalent Mach numbers from approximately 6.5 to 9.5, depending on GN₂ injection rate, standoff distance, and body shape.
- Simultaneous acquisition of high-quality surface pressure distributions, stagnation pressures, and optical temperature histories, providing a dataset suitable for CFD code validation and preliminary material response screening.

The most significant technical outcome is the ability to produce flight-relevant total enthalpy at non-negligible freestream density (and hence meaningful dynamic pressure) for burn durations of 4–10 seconds in a university-scale laboratory for a small fraction of the cost and schedule required by traditional high-enthalpy facilities. This combination of enthalpy, dynamic pressure, and test duration is currently unavailable in any continuously operating ground-test asset worldwide.

The broader implications of this capability are substantial. First, it offers a rapid, affordable platform for validating CFD models of hypersonic separated flows, shock/boundary-layer interaction, and real-gas effects—areas where even state-of-the-art numerical tools continue to exhibit deficiencies. Second, the method enables early-stage material survivability screening and sensor development under combined aerodynamic and thermal loads that more closely

mimic actual flight than pure arc-jet testing. Third, the inherent tunability of the system — through variation of O/F ratio, chamber pressure, GN₂ injection rate, standoff distance, and even propellant selection (e.g., future transition to N₂O/ABS or other thermoplastic grains) — provides a versatile “hypersonic wind-tunnel-in-a-box” that can simulate a wide range of altitudes and trajectory points.

Future extensions of this platform are numerous and straightforward. Substitution of nitrous oxide for GOX is expected to yield combustion products with species mass fractions even closer to air while naturally lowering flame temperature, permitting longer burn times and higher chamber pressures for increased total enthalpy. Incorporation of trace species (argon, CO₂, or water vapor) via secondary injection can further tailor the gas composition to specific altitude conditions. Inclusion of a digital throttle in the secondary injection line could simulate an entire re-entry trajectory. Coupling the gas generator to a larger test stand could extend test times beyond 30 seconds, approaching quasi-steady conditions suitable for ablation and boundary-layer transition studies.

Ultimately, the hybrid-rocket-based gas generator presented here represents a potentially market-disruptive alternative to traditional high-enthalpy test infrastructure. By dramatically lowering the cost and access barriers to flight-relevant hypersonic ground testing, it has the potential to accelerate design iteration cycles, improve confidence in computational models, mature lower-TRL concepts earlier in the development pipeline, and significantly reduce risk before committing to expensive campaigns in national shock-tunnel or arc-jet facilities. In an era of renewed strategic emphasis on sustained hypersonic flight, affordable and flexible test capabilities such as this are not merely convenient—they are essential enablers of rapid, reliable technology maturation.

Appendices

A. Temperature Calculation from Plume Spectra Data

Temperature at the stagnation point is calculated using recorded plume spectra. A calibration of spectrometers against a reference source is needed to anchor spectra measurements. This section outlines the calibration process, which involves a wavelength calibration using narrow-band filters, computation of the instrument's transfer function, and a Wiener deconvolution to reconstruct the true spectra. The methodology is implemented in MATLAB, with results visualized through spectral plots.

Three spectrometers with varying wavelength ranges are used to obtain a visible and partial near-infrared (NIR) spectra. The spectrometers are LR1, Qmini, and Qneo and the respective wavelength ranges are shown in Table A1.

Table A1 Spectrometers and Associated Wavelength Range

Spectrometer	Manufacturer	Wavelength Range (nm)
LR1	ASEQ Instruments	150 - 1200
Qmini	Broadcom	480 - 1100
Qneo	Broadcom	950 - 1700

A. Wavelength Calibration

Wavelength calibration corrects the spectrometer's wavelength axis to align with true wavelengths, as the raw wavelength data from the spectrometer may exhibit systematic errors due to sensor characteristics. The process uses narrow-band filters with nominal center wavelengths at 450, 550, 650, 750, 850, 1000, 1200, 1400, and 1600 nm. For each filter, the spectra is measured and stored in an .lvm file, containing amplitude data across wavelengths and timestamps. The mean amplitude across timestamps is computed to obtain a representative spectrum for each filter:

$$\bar{a}_i(\lambda) = \frac{1}{N} \sum_{j=1}^N a_i(\lambda, t_j), \quad (\text{A1})$$

where $\bar{a}_i(\lambda)$ is the mean amplitude for the i -th filter, $a_i(\lambda, t_j)$ is the amplitude at wavelength λ and time t_j , and N is the number of timestamps. Similar to the process described in [6], the centroid wavelength for each narrow-band filter is calculated to represent the filter's effective wavelength. The centroid wavelength $\lambda_{\text{centroid},i}$ is the intensity-weighted mean:

$$\lambda_{\text{centroid},i} = \frac{\sum_k (\lambda_k \cdot \bar{a}_i(\lambda_k))}{\sum_k \bar{a}_i(\lambda_k)}, \quad (\text{A2})$$

where λ_k are the wavelength points in the filter's spectrum, and $\bar{a}_i(\lambda_k)$ is the mean amplitude at λ_k . The centroid wavelengths ($\lambda_{\text{centroid},i}$) are paired with the nominal wavelengths to form a calibration dataset. A linear model is fitted to map sensed wavelengths to true wavelengths:

$$\lambda_{\text{true},i} = c_1 \cdot \lambda_{\text{centroid},i} + c_2, \quad (\text{A3})$$

where c_1 and c_2 are the slope and intercept, determined using least-squares regression. The spectrometer wavelength response is approximately linear across its range [6], making a linear model appropriate. The calibrated wavelength grid is computed as:

$$\lambda_{\text{calibrated}} = c_1 \cdot \lambda_{\text{measured}} + c_2, \quad (\text{A4})$$

where $\lambda_{\text{measured}}$ is the measured wavelength array from the spectrometer. All wavelength-dependent variables (e.g., mean spectrum, noise, signal-to-noise ratio, and transfer function) are interpolated to the new calibrated grid using linear interpolation with extrapolation for edge points:

$$f(\lambda_{\text{calibrated}}) = \text{interp1}(\lambda, f(\lambda), \lambda_{\text{calibrated}}, \text{'linear'}, \text{'extrap'}), \quad (\text{A5})$$

where $f(\lambda)$ represents any wavelength-dependent function. Fig. A1 shows the LR1 main spectrum and filter spectra on the calibrated wavelength grid.

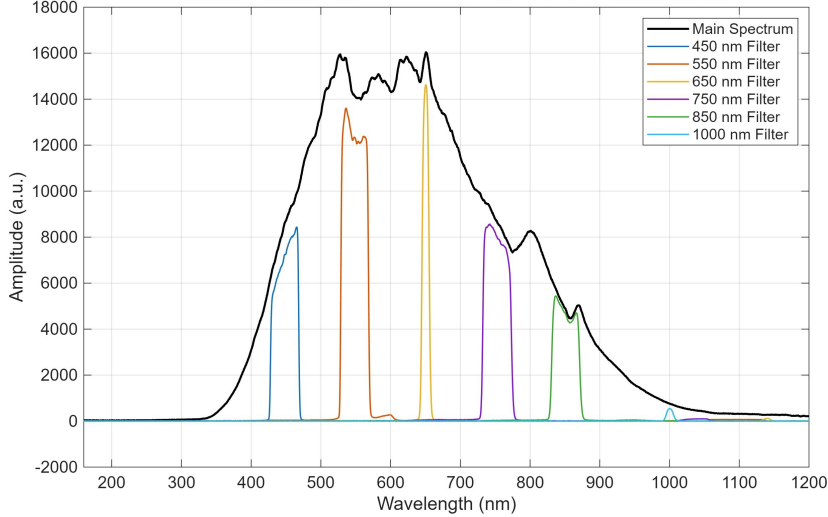


Fig. A1 LR1 main spectrum and narrow-band filter spectra after wavelength calibration.

B. Noise Estimation

Noise characterization is essential for quantifying spectral variability and informing the Wiener deconvolution process. Noise is estimated from the high-frequency content removed by smoothing each individual spectrum. For every wavelength λ , the spectrum is smoothed using a Savitzky–Golay filter. The absolute difference between the raw and smoothed spectrum at each timestamp defines the instantaneous noise and is shown in Eq. (A6). The mean noise across all timestamps is then computed in Eq. (A7).

$$N(\lambda, t) = |a(\lambda, t) - a_{\text{smoothed}}(\lambda, t)| \quad (\text{A6})$$

$$\bar{N}(\lambda) = \frac{1}{N} \sum N(\lambda, t) \quad (\text{A7})$$

Heavy smoothing is subsequently applied to $\bar{N}(\lambda)$ using a Savitzky–Golay filter to produce the final noise estimate $N_{\text{smoothed}}(\lambda)$. This approach captures spectral noise structure more effectively than temporal variance for stable tungsten source measurements. Fig. A2 shows the raw mean noise and the heavily smoothed noise profile for the LR1.

The signal-to-noise ratio is computed from the smoothed mean spectrum and smoothed noise:

$$\text{SNR}(\lambda) = \left[\frac{S_{m, \text{smoothed}}(\lambda)}{N_{\text{smoothed}}(\lambda) + \epsilon} \right]^2 \quad (\text{A8})$$

where ϵ is a conditioning coefficient to eliminate division by zero. A Savitzky–Golay filter is applied to reduce residual fluctuations in $\text{SNR}(\lambda)$. Fig. A3 shows the raw and smoothed SNR on the calibrated wavelength grid for the LR1. It is important to note that Savitzky–Golay filters convolute and "smear" the measured data, causing loss of detail for some of the artifacts inherent to the system ie. spectrometers, fiber optic cables, etc. It is more advantageous to remove the noise from the measured spectra through excess smoothing and lose the aforementioned system artifacts. The spectrometers' low sampling rate (approximately 6 Hz), combined with the practical challenges of conducting a large number of hot-fire tests, prevents acquisition of sufficient measured spectra to effectively reduce random noise through statistical averaging.

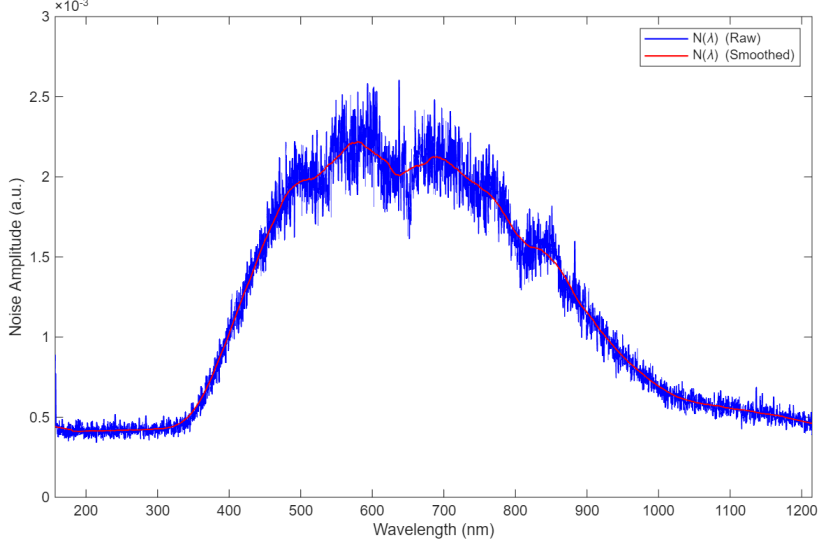


Fig. A2 LR1 Raw and smooth noise vs. wavelength on the calibrated grid.

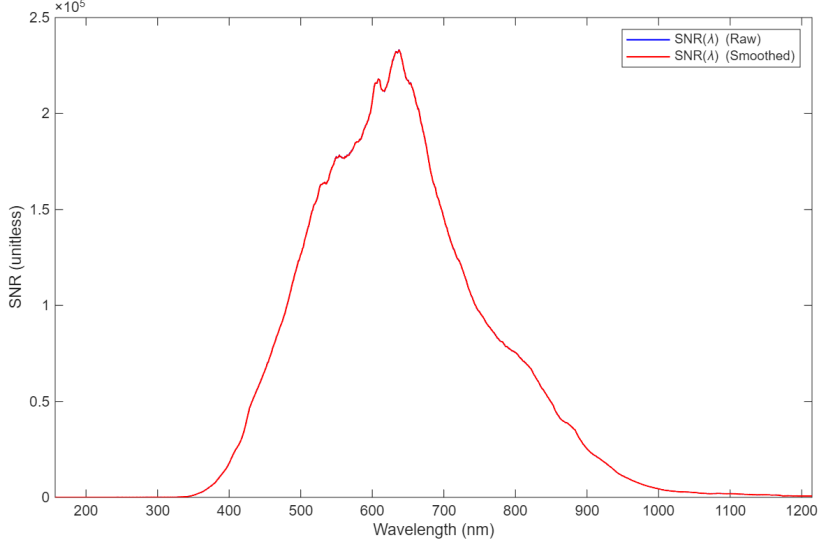


Fig. A3 LR1 Raw and smooth signal-to-noise ratio vs. wavelength on the calibrated grid.

C. Transfer Function Computation

The transfer function $\Upsilon(\lambda)$ models the spectrometer's response, relating the measured mean spectrum $\bar{S}_m(\lambda)$ to the true spectrum $S_t(\lambda)$:

$$\bar{S}_m(\lambda) = \Upsilon(\lambda)S_t(\lambda) \quad (\text{A9})$$

A Tungsten-Halogen light source provides a blackbody radiation spectrum from 350 nm to 2600 nm at 2796 K. Using the reference tungsten spectrum extended from 160-349 nm using Planck's blackbody radiation law scaled to match the measured value at 350 nm, the transfer function is computed and smoothed with a Savitzky–Golay filter to suppress noise before use in the Wiener filter.

D. Wiener Deconvolution

A spectrally varying Wiener filter is constructed using the estimated SNR. The deconvolution filter is:

$$\Upsilon_{\text{Wiener}}(\lambda) = \frac{\Upsilon_{\text{smoothed}}(\lambda) \cdot \text{SNR}_{\text{smoothed}}(\lambda)}{\Upsilon_{\text{smoothed}}(\lambda)^2 \cdot \text{SNR}_{\text{smoothed}}(\lambda) + 1} \quad (\text{A10})$$

This form naturally suppresses deconvolution in low-SNR regions while preserving high-fidelity regions. The reconstructed spectrum is obtained by:

$$S(\lambda) = \Upsilon_{\text{Wiener}}(\lambda) \cdot S_{m,\text{smoothed}}(\lambda) \quad (\text{A11})$$

The result is normalized to unit peak amplitude. The transfer function after wiener deconvolution is shown in Fig. A4.

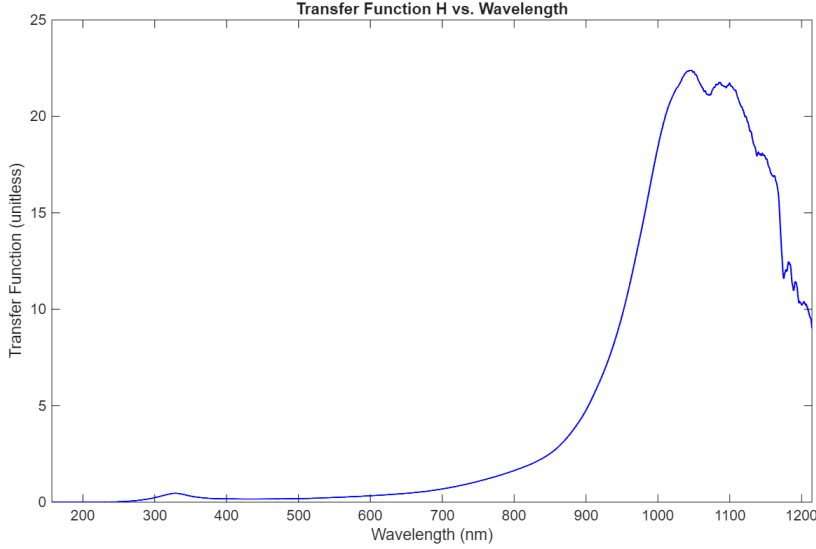


Fig. A4 Wiener deconvolution vs. wavelength on the calibrated grid.

E. Planck's Law Curve Fitting

With the fully calibrated and Wiener-deconvolved spectrum now representing the true spectral radiance of the tungsten calibration source, a blackbody temperature is extracted by fitting Planck's radiation law over the 300–1100 nm range where the spectrometer response is reliable. This method assumes a blackbody fit is a sufficient estimate for the hybrid rocket plume. Future work will involve verification of this assumption.

Planck's law for spectral radiance (in wavelength) is:

$$B(\lambda, T) = \frac{2h_p v_{light}^2}{\lambda^5} \frac{1}{\exp\left(\frac{h_p v_{light}}{\lambda k_B T}\right) - 1}, \quad (\text{A12})$$

where $h_p = 6.62607015 \times 10^{-34}$ J s, $v_{light} = 2.99792458 \times 10^8$ m/s, and $k_B = 1.380649 \times 10^{-23}$ J/K are Planck's constant, the speed of light, and Boltzmann's constant, respectively.

Because only a single scaling factor and temperature are unknown, the measured spectrum is fit by minimizing the weighted reduced- χ^2 statistic

$$\chi^2(T, A) = \sum_i w_i [S(\lambda_i) - A \cdot B(\lambda_i, T)]^2, \quad (\text{A13})$$

where A is a free amplitude parameter that accounts for unknown collection solid angle and integration time, and the weights are chosen as $w_i = \text{SNR}_{\text{smoothed}}^2(\lambda_i)$ to emphasize high signal-to-noise regions.

The optimal temperature T is found using MATLAB's `fminsearch` routine initialized near the user set temperature. The fit converges to the best fit curve where an amplitude is clear. Wien's displacement law is then applied to verify the converged temperature value:

$$T = \frac{b}{\lambda_{\max}} \quad (\text{A14})$$

where b is the Wien's displacement constant ($2898 \mu\text{m} \cdot \text{K}$). Generally, the calculated temperature matches the Planck's Law temperature within 10–12 K [6].

This blackbody fit serves as an independent end-to-end validation of the entire calibration chain: wavelength calibration, noise estimation, transfer function correction, and Wiener deconvolution. The retrieved temperature from the calibration is within 10 K of the manufacturer-specified color temperature of the Tungsten-Halogen source source, confirming radiometric accuracy across the 160–1200 nm band.

B. Temperature and Enthalpy Analysis

This Appendix Derives the one-dimensional model for the mixed-flow plume and GN₂ enthalpy and flow temperature. The technique used to calculate the mixed-flow thermodynamic transport properties is also presented.

A. Mixed-Flow Enthalpy Analysis

Table B1 defines the parameters to be considered in this analysis.

Table B1 Terms and parameters used for post-nozzle enthalpy and dilution analysis

Parameter	Motor Plume Exit Flow	GN ₂ Injection Flow	Mixed Flow
Mass flow rate (g/s)	\dot{m}_e	\dot{m}_{GN_2}	—
Longitudinal velocity (m/s)	v_e	—	v_2
Kinetic energy (J)	(K.E.) _e	—	(K.E.) ₂
Total enthalpy (J/s)	(H_0) _e	H_{GN_2}	$H_{0,2}$
Temperature (K)	$T_{0,e}$	T_{GN_2}	T_2
Specific heat (J/kg-K)	$C_{p,e}$	C_{p,GN_2}	C_{p2}
Fraction decomposition	—	$\mathcal{E}_{\text{GN}_2}$	—
Enthalpy of decomposition (J/kg)	—	J_{decomp}	—

1. Mixed Flow Kinetic Energy

The model starts by considering the conservation of longitudinal flow momentum. Because the GN₂ flow is injected perpendicular to the main plume, it does not directly increase total flow momentum. Thus, the momentum balance is

$$\dot{m}_e \cdot v_e = (\dot{m}_e + \dot{m}_{\text{GN}_2}) \cdot v_2. \quad (\text{B1})$$

Solving for the downstream (mixed flow) velocity v_2 ,

$$v_2 = \frac{\dot{m}_e}{\dot{m}_e + \dot{m}_{\text{GN}_2}} \cdot v_e. \quad (\text{B2})$$

Similarly, since the GN₂ injection adds no kinetic energy to the longitudinal flow stream, the kinetic energy of the combined stream is

$$(K.E.)_2 = \frac{1}{2}(\dot{m}_e + \dot{m}_{\text{GN}_2}) \cdot v_2^2 \quad (\text{B3})$$

Substituting for v_2 into Eq. (B3),

$$(K.E.)_2 = \frac{1}{2}(\dot{m}_e + \dot{m}_{\text{GN}_2})v_2^2 = \frac{1}{2}(\dot{m}_e + \dot{m}_{\text{GN}_2}) \left(\frac{\dot{m}_e}{\dot{m}_e + \dot{m}_{\text{GN}_2}} \right)^2 \cdot v_e^2. \quad (\text{B4})$$

Simplifying and collecting terms,

$$(K.E.)_2 = \frac{1}{2}\dot{m}_e v_e^2 \left(\frac{\dot{m}_e}{\dot{m}_e + \dot{m}_{\text{GN}_2}} \right). \quad (\text{B5})$$

Since the kinetic energy of the nozzle exit plane is

$$(K.E.)_e = \frac{1}{2} \dot{m}_e v_e^2, \quad (B6)$$

the mixed-flow kinetic energy can be written in terms of the exit plane kinetic energy:

$$(K.E.)_2 = (K.E.)_e \left(\frac{\dot{m}_e}{\dot{m}_e + \dot{m}_{GN_2}} \right). \quad (B7)$$

2. Mixed Flow Total Enthalpy

The total enthalpy at the nozzle exit plane is

$$H_e = H_{0,e} = \dot{m}_e \cdot C_{p,e} \cdot T_{0,e} = \dot{m}_e \cdot (C_{p,e} \cdot T_e + \frac{1}{2} \cdot v_e^2). \quad (B8)$$

The total enthalpy of the GN_2 injection stream is

$$H_{GN_2} = \dot{m}_{GN_2} \cdot C_{p,GN_2} \cdot T_{GN_2}. \quad (B9)$$

Adding the total enthalpies to calculate the enthalpy of the combined stream,

$$H_{0,2} = \dot{m}_e \cdot C_{p,e} \cdot T_{0,c} + \dot{m}_{GN_2} \cdot C_{p,GN_2} \cdot T_{GN_2} = (\dot{m}_e + \dot{m}_{GN_2}) \cdot C_{p,2} \cdot T_2 + (K.E.)_2 \quad (B10)$$

Allowing for the thermal decomposition of the GN_2 at the high exhaust temperatures,

$$(\Delta H_0)_{GN_2,decomp} = -\frac{\dot{m}_{GN_2,decomp}}{MW_{GN_2}} \cdot J_{decomp} = \epsilon_{GN_2,decomp} \cdot J_{decomp} \cdot \frac{\dot{m}_{GN_2}}{MW_{GN_2}}. \quad (B11)$$

In Eq. (B11), the dimensional values of the parameters are

$$\begin{aligned} J_{decomp} &= 0.94488 \text{ kJ/g-mol} \\ MW_{GN_2} &= 28.014 \text{ kJ/g-mol}. \end{aligned}$$

Subtracting decomposition enthalpy from total enthalpy gives

$$H_{O_2} = \dot{m}_e \cdot C_{p,e} \cdot T_{0,c} + \dot{m}_{GN_2} \cdot C_{p,GN_2} \cdot T_{GN_2} - (\Delta H_0)_{GN_2,decomp} = (\dot{m}_e + \dot{m}_{GN_2}) \cdot C_{p,2} \cdot T_2 + (K.E.)_2. \quad (B12)$$

Solving Eq. (B12) for combined flow temperature in the mixed-flow plume gives,

$$T_2 = \frac{\dot{m}_e \cdot C_{p,e} \cdot T_{0,c} + \dot{m}_{GN_2} \cdot C_{p,GN_2} \cdot T_{GN_2} - (\Delta H_0)_{GN_2,decomp} - (K.E.)_2}{(\dot{m}_e + \dot{m}_{GN_2}) \cdot C_{p,2}} \quad (B13)$$

3. Calculating the Mixed-Flow Thermodynamic and Transport Properties

The thermodynamic parameters of the mixed-flow plume are calculated using the methods outlined by Whitmore et al. [5]. First, the exhaust-gas properties—such as the ratio of specific heats (γ), molecular weight (MW), specific heat (C_p), specific gas constant (R), stagnation temperature (T_0), and exit temperature (T_e)—are determined using the NASA CEA computer code [26]. Tables of properties with combustion efficiency η^* , oxidizer-to-fuel (O/F) ratio, and chamber pressure P_0 as independent lookup variables were developed for the GOX/ABS propellant combination. Next, the GN_2 injection mass flow rate is calculated from the measured manifold exit pressure and the known injector orifice characteristics. The nozzle exit plane and GN_2 mass flow rates are subsequently used to calculate the relative molar flow proportions. The mixed-flow molecular weight is then calculated using Dalton's law [27].

$$\overline{MW} = \frac{\sum_j (n_j \cdot MW_j)}{\sum_j n_j} \quad (B14)$$

In Eq. (B14), the parameter n_j represents the molar proportions of each constituent species (exhaust plume and GN₂ gases). MW_j represents the respective molecular weights. The molar specific heat of the mixed flow is then calculated from the individual molar specific heats,

$$\bar{C}'_p = \frac{\sum_j (n_j \cdot C'_{p,j})}{\sum_j (n_j)}. \quad (\text{B15})$$

In Eq. (B15), the molar specific heat is calculated from the mass specific heat by

$$(C'_p)_j = (MW_j \cdot C'_p)_j. \quad (\text{B16})$$

The mass specific heat for the mixed flow is then subsequently calculated by

$$\bar{C}_p = \frac{\bar{C}'_p}{\bar{M}W}. \quad (\text{B17})$$

This calculation is repeated for both the specific heat at constant pressure \bar{C}_p and specific heat at constant volume \bar{C}_v , and the associated mixed-flow γ is calculated from the ratio,

$$\bar{\gamma} = \frac{\bar{C}_p}{\bar{C}_v}. \quad (\text{B18})$$

The associated mixed-flow gas constant is calculated by

$$\bar{R}_g = \frac{R_u}{\bar{M}W}, \quad (\text{B19})$$

where $R_u = 8.314\,46 \text{ J/kg}\cdot\text{K}$ is the universal ideal-gas constant.

Acknowledgments

The authors would like to thank the NASA Small Spacecraft Technology Program for funding this work, and the NASA Marshall Space Flight Center for supporting this development testing. Due to the previously published, legacy, nature of the test hardware used for this study, this work is published under the Fundamental Research Exclusion [28], which allows general scientific, mathematical, or engineering principles commonly taught in schools, colleges, and universities, or information in the public domain, to be published without specific US government authorization. Space Systems LLC. This material is based upon work conducted under the Fundamental Research Exclusion and is approved for public release.

References

- [1] Shang, J. J. S., and Yan, H., “High-enthalpy hypersonic flows,” *Advances in Aerodynamics*, Vol. 2, No. 19, 2020. <https://doi.org/10.1186/s42774-020-00041-y>, Accessed 3 December 2025.
- [2] Gu, S., and Olivier, H., “Capabilities and limitations of existing hypersonic facilities,” *Progress in Aerospace Sciences*, Vol. 113, 2020, p. 100607. <https://doi.org/10.1016/j.paerosci.2020.100607>, Accessed 3 December 2025.
- [3] Lyczkowski, R. W., *The Rise of the First Commercial CFD Codes: PHOENICS, FLUENT, FIDAP, CFX, FLOW-3D, and STAR-CD*, Springer International Publishing, 2018, pp. 185–187. https://doi.org/10.1007/978-3-319-66502-3_14, Accessed 3 December 2025.
- [4] Knight, D., Longo, J., Drikakis, D., Gaitonde, D., Lani, A., Nompelis, I., Reimann, B., and Walpot, L., “Assessment of CFD capability for prediction of hypersonic shock interactions,” *Progress in Aerospace Sciences*, Vol. 48-49, 2012, pp. 8–26. <https://doi.org/10.1016/j.paerosci.2011.10.001>, assessment of Aerothermodynamic Flight Prediction Tools.
- [5] Whitmore, S. A., and Thibaudeau, R. J., “Feasibility Assessment of a High-Enthalpy Test Capability Using a Green-Propellant Hybrid Gas Generator,” *AIAA SCITECH 2025 Forum*, 2025. <https://doi.org/10.2514/6.2025-1443>, Accessed 3 December 2025.
- [6] Whitmore, S. A., Borealis, C. I., and Francom, M. W., “Minimally-intrusive, dual-band, fiber-optic sensing system for high-enthalpy exhaust plumes,” *Electronic Research Archive*, Vol. 32, No. 4, 2024, pp. 2541–2597. <https://doi.org/10.3934/era.2024117>, Accessed 3 December 2025.
- [7] “Rankine Oval,” , 2005. URL https://www-mdp.eng.cam.ac.uk/web/library/enginfo/aero/thermal_dvd_only/aero/fprops/poten/node36.html, Accessed 3 December 2025.
- [8] Whitmore, S. A., and Thibaudeau, R. J., “Development of a GOX/ABS Hybrid-Gas Generator System for the NASA Plume Surface Interaction (PSI) Experimental Campaign,” *AIAA SciTech 2026 Forum*, Orlando, FL, USA, 2026. Companion paper describing the PSI hybrid gas-generator test campaign. Report number and URL TBD.
- [9] Whitmore, S. A., Babb, R. S., Gardner, T. J., LLoyd, K. P., and Stephens, J. C., “Pyrolytic Graphite and Boron Nitride as Low-Erosion Nozzle Materials for Long-Duration Hybrid Rocket Testing,” *AIAA Propulsion and Energy 2020 Forum*, 2020. <https://doi.org/10.2514/6.2020-3740>, Accessed 3 December 2025.
- [10] Whitmore, S. A., Inkley, N. R., Merkley, D. P., and Judson, M. I., “Development of a Power-Efficient, Restart-Capable Arc Ignitor for Hybrid Rockets,” *Journal of Propulsion and Power*, Vol. 31, No. 6, 2015, pp. 1739–1749. <https://doi.org/10.2514/1.B35595>, Accessed 3 December 2025.
- [11] Whitmore, S. A., Merkley, S. L., Tonic, L., and Mathias, S. D., “Survey of Selected Additively Manufactured Propellants for Arc Ignition of Hybrid Rockets,” *Journal of Propulsion and Power*, Vol. 32, No. 6, 2016, pp. 1494–1504. <https://doi.org/10.2514/1.B36106>, Accessed 3 December 2025.
- [12] Whitmore, S. A., Mathias, S., and Harvey, R., “High Voltage Breakdown and Arc-Tracking Mechanism of Thermoplastics with Applications to Hybrid Rocket Arc- Ignition,” *53rd AIAA/SAE/ASEE Joint Propulsion Conference*, 2017, p. 4601. <https://doi.org/10.2514/6.2017-4601>, Accessed 3 December 2025.
- [13] “C Series Capacitive Charging, DC-DC Power Supplies,” , n.d. URL [https://www.advancedenergy.com/en-us/products/dc-dc-conversion-products/high-voltage-boost-\(u-v\)/single-o-p-\(to-30w-40kv\)/c-series/](https://www.advancedenergy.com/en-us/products/dc-dc-conversion-products/high-voltage-boost-(u-v)/single-o-p-(to-30w-40kv)/c-series/), Product datasheet. Accessed 3 December 2025.
- [14] Whitmore, S. A., and Bulcher, A. M., “Vacuum Test of a Novel Green-Propellant Thruster for Small Spacecraft,” *53rd AIAA/SAE/ASEE Joint Propulsion Conference*, 2017, p. 5044. <https://doi.org/10.2514/6.2017-5044>, Accessed 3 December 2025.

- [15] Sorenson, J. R., Mecham, L. J., White, C. A., and Wilkey, A. T., “Refined Hybrid Rocket Static Fire Testing with Increased Performance and Precision,” *Conference on Characterization and Radiometric Calibration for Remote Sensing (CALCON) 2025*, Utah State University, Logan, UT, USA, 2025. URL <https://digitalcommons.usu.edu/calcon/CALCON2025>All2025Content/20/>, Accessed 3 December 2025.
- [16] “9000 Series Intelligent Pressure Scanners User’s Manual,” , 1998. URL <https://engineering.purdue.edu/~aae520/9000manual.pdf>, Product datasheet. Accessed 3 December 2025.
- [17] Whitmore, S. A., Frischkorn, C. I., and Peterson, S., “In-Situ Optical Measurements of a GOX/ABS Hybrid Rocket Plume,” *AIAA SCITECH 2022 Forum*, 2022, p. 0771. <https://doi.org/10.2514/6.2022-0771>, Accessed 3 December 2025.
- [18] Whitmore, S. A., Frischkorn, C. I., and Peterson, S., “In-Situ Optical Measurements of Solid and Hybrid-Propellant Combustion Plumes,” *Aerospace*, Vol. 9, No. 2, 2022. <https://doi.org/10.3390/aerospace9020057>, Accessed 3 December 2025.
- [19] “LR1 Broad Range Spectrometer,” , n.d. URL <https://www.aseq-instruments.com/>, Product information. Accessed 3 December 2025.
- [20] “Spectrometers Qmini,” , n.d. URL <https://www.broadcom.com/products/optical-sensors/spectrometers/spectrometers-qmini>, Product information. Accessed 3 December 2025.
- [21] “Spectrometers Qneo,” , n.d. URL <https://www.broadcom.com/products/optical-sensors/spectrometers/spectrometers-qneo>, Product information. Accessed 3 December 2025.
- [22] Dougal, R. C., “The presentation of the Planck radiation formula (tutorial),” *Physics Education*, Vol. 11, No. 6, 1976, p. 438. <https://doi.org/10.1088/0031-9120/11/6/008>, Accessed 3 December 2025.
- [23] Halliday, D., Resnick, R., and Walker, J., *Fundamentals of Physics Extended 8th*, 8th ed., John Wiley and Sons, 2007, p. 891. ISBN 978-0-471-75801-3.
- [24] Whitmore, S. A., Peterson, Z. W., and Eilers, S. D., “Comparing Hydroxyl Terminated Polybutadiene and Acrylonitrile Butadiene Styrene as Hybrid Rocket Fuels,” *Journal of Propulsion and Power*, Vol. 29, No. 3, 2013. <https://doi.org/10.2514/1.B34382>.
- [25] Anderson, J. D., *Modern Compressible Flow with a Historical Perspective*, 3rd ed., McGraw Hill, 2003. ISBN 978-0072424430.
- [26] Gordon, S., and McBride, B. J., “Computer Program for Calculation of Complex Chemical Equilibrium Compositions and Applications. I. Analysis,” Tech. Rep. NASA RP-1311, National Aeronautics and Space Administration, Cleveland, OH, 1994. URL <https://ntrs.nasa.gov/api/citations/19950013764/downloads/19950013764.pdf>, NASA Reference Publication 1311. Accessed 3 December 2025.
- [27] Silberberg, M. S., *Chemistry: The Molecular Nature of Matter and Change*, 5th ed., McGraw Hill, 2009.
- [28] “National Policy on the Transfer of Scientific, Technical and Engineering Information,” 1985. URL <https://irp.fas.org/offdocs/nsdd/nsdd-189.htm>.